



**23 Abstract**

24 Seafloor massive sulfide deposits form in remote environments, and the assessment of deposit  
25 size and composition through drilling is technically challenging and expensive. To aid the  
26 evaluation of the resource potential of seafloor massive sulfide deposits, three-dimensional  
27 inverse modelling of geophysical potential field data (magnetic and gravity) collected near the  
28 seafloor can be carried out to further enhance geologic models interpolated from sparse drilling.  
29 Here, we present inverse modelling results of magnetic and gravity data collected from the active  
30 mound at the Trans-Atlantic Geotraverse hydrothermal vent field, located at 26°08'N on the Mid-  
31 Atlantic Ridge, using autonomous underwater vehicle (AUV) and submersible surveying. Both  
32 minimum-structure and surface geometry inverse modelling methods were utilized. Through  
33 deposit-scale magnetic modelling, the outer extent of a chloritized alteration zone within the  
34 basalt host rock below the mound was resolved, providing an indication of the angle of the rising  
35 hydrothermal fluid and the depth and volume of seawater/hydrothermal mixing zone. The  
36 thickness of the massive sulfide mound was determined by modelling the gravity data, enabling  
37 the tonnage of the mound to be estimated at 2.17 +/- 0.44 Mt through this geophysics-based,  
38 non-invasive approach.

39

**40 Plain Language Summary**

41 As the exploration and exploitation of seafloor polymetallic deposits appears to be the next  
42 frontier in mineral exploration, developing and optimizing remote sensing methods to locate and  
43 study these deposits is becoming increasingly important for understanding the resource potential  
44 and environmental implications of mining from the deep seafloor. One such deposit type is the  
45 seafloor massive sulfide (SMS) deposit, which forms on and below the seafloor and are  
46 commonly seen as “black smoker” chimney mounds. SMS deposits have promise to offer new  
47 sources of Cu, Zn, Pb, Au, and Ag, but the remote environment in which they are located creates  
48 difficulties for their discovery and resource estimates. Drilling these deposits are expensive, and  
49 unless drillcores are collected in large numbers, and to sufficient depth, they will offer limited  
50 geometric information of the deposit. Alternatively, magnetic and gravity data collected over  
51 SMS deposits can be modelled to derive 3D deposit models. These sorts of models will be able  
52 to better design initial assessments of SMS deposits so that future drilling can be better informed

53 and more efficient. This study presents magnetic and gravity models of the Trans-Atlantic  
54 Geotraverse active mound, updating its tonnage estimate to 2.17 +/- 0.44 Mt.

55

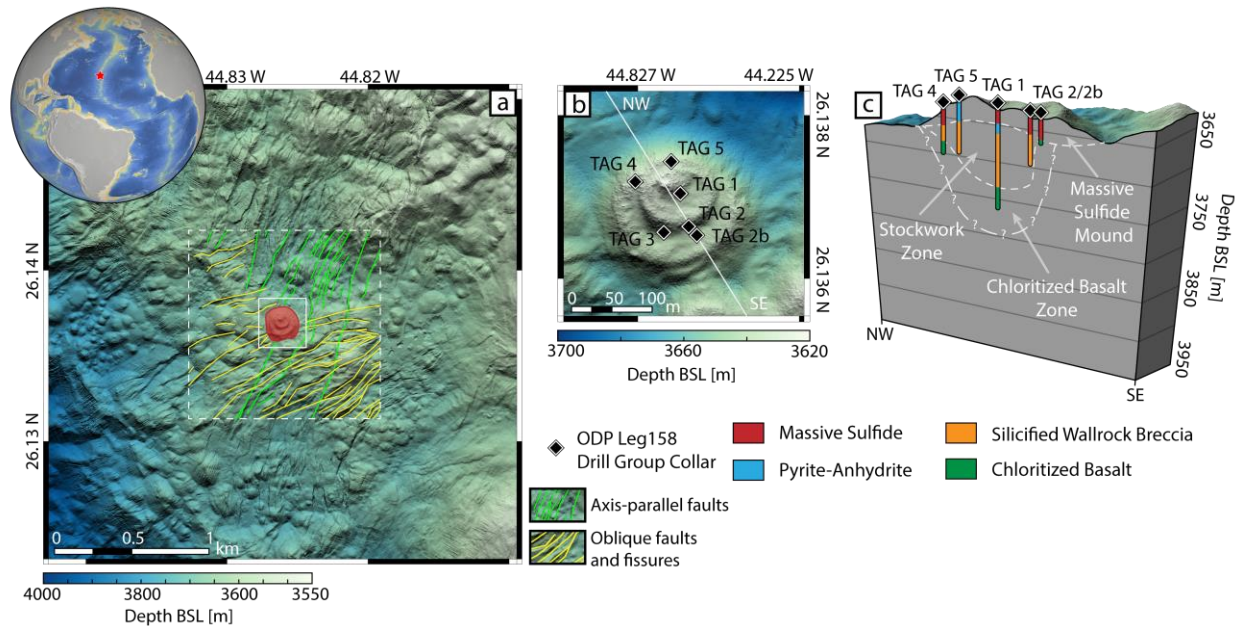
## 56 **1 Introduction**

57 Seafloor massive sulfide (SMS) deposits form at the seafloor at sites of high-temperature  
58 hydrothermal venting. These metal-rich deposits represent the modern equivalents of ancient  
59 volcanogenic massive sulfide (VMS) deposits, and serve as a potential future source for copper,  
60 gold, silver, zinc, and lead (Hannington et al., 2011). They form at or near the seafloor by the  
61 precipitation of sulfide minerals from metal-laden hydrothermal fluids, where the remote  
62 environment and hostile conditions make conventional deposit assessment methods such as  
63 drilling challenging and expensive.

64 The Trans-Atlantic Geotraverse (TAG) active mound is a hydrothermally active SMS deposit  
65 located on the hanging wall of a detachment fault at 26°08'N along the Mid-Atlantic Ridge (Fig.  
66 1; Rona et al., 1993; Tivey et al., 2003). The TAG mound is composed primarily of massive  
67 sulfide and anhydrite (Petersen et al., 2000). Drilling of the active mound was conducted in 1994  
68 as part of the Ocean Drilling Program (ODP) Leg 158, from which a mineralogical  
69 reconstruction of the active mound's massive sulfide and sulfate interior, silicified wallrock  
70 breccia, and chloritized basalt unit was created (Knott et al., 1998; Smith & Humphris, 1998).  
71 The deposit's outer most subseafloor alteration unit, the chloritized basalt, was intersected by  
72 three of the Leg 158 boreholes (TAG 1, 2b, and 4), but those boreholes did not penetrate deep  
73 enough to intersect the contact between the chloritized basalt and unaltered basalt. This  
74 chloritization of the seafloor is an alteration process that occurs as a result of the rising  
75 hydrothermal fluids mixing with the more magnesium rich local seawater at > 200°C (Galley &  
76 Koski, 1999; Humphris et al., 1998; Seyfried & Bischoff, 1981). Information regarding the depth  
77 and scale of the local seawater circulation into the TAG hydrothermal system could be derived

78 from the geometry and size of the chloritized basalt unit, which in turn can be used to  
 79 approximate the maximum size of the deposit.

80



81

82 **Figure 1. a)** The bathymetric map of the study area. The regional inversion model's volume of  
 83 interest is outlined with a dotted white line, whereas the volume of interest for the deposit scale  
 84 inversion is outlined by a solid white line. Structural information is from Graber et al. (2020); **b)**  
 85 Map of the TAG active mound showing locations of the ODP Leg 158 boreholes; **c)** borehole  
 86 lithology logs from Knott et al. (1998) projected onto a NW/SE cross section (white line in b).  
 87 Bathymetric data with 2 m resolution was collected in 2016 using the GEOMAR AUV *Abbyss*  
 88 (Petersen and Shipboard Scientific Party, 2016).

89

90 The rising hydrothermal fluids and their associated seafloor alteration have multiple effects on  
 91 the physical properties of the crust. The hydrothermal fluids increase the rate of titanium and  
 92 ferrous iron dissolution from the titanomagnetites, the primary magnetic mineral, and to a lesser  
 93 degree increase the oxidation of the titanomagnetites, making SMS deposits low magnetic  
 94 anomalies both at the seafloor and deep into the crust (Sztikar et al., 2014; Wang et al., 2020).  
 95 On the deposit scale all lithologic zones (i.e. the massive sulfide mound and the stockwork zone;

96 Fig. 1c) within the chloritized basalt unit contain the lowest magnetization and magnetic  
97 susceptibilities (Wang et al., 2020), with a secondary magnetic low extending down the length of  
98 the hydrothermal fluid upflow zone due to the hydrothermally altered crust (Galley et al., 2020a).  
99 Despite the TAG mound being a homogeneous magnetic low, its massive sulfide mound unit can  
100 be distinguished from the other units by its anomalously high density (Evans, 1996; Ludwig et  
101 al., 1998), caused by its primary composition of massive sulfide (with a density of approximately  
102  $3.65 \text{ g/cm}^3$  compared to  $2.4 \text{ g/cm}^3$  for basalt; Evans, 1996).

103 Investigations of the seafloor structure of SMS deposits have been mainly driven by drilling.  
104 The sparse drilling at the TAG active mound has provided key information on the geometry  
105 (Humphris et al., 1995) and genesis of SMS and VMS deposits (You & Bickle, 1998), and has  
106 led to the TAG active mound model to be widely used as a representative for a generic SMS  
107 deposit (Galley et al., 2007; Herzig & Hannington, 1995). However, the geological interpretation  
108 of the TAG active mound was primarily two-dimensional (2D), with only one borehole (TAG 1)  
109 extending deep (approximately 120 m) into the deposit's core (Knott et al., 1998). The overall  
110 drilling was therefore not deep enough to determine the thickness of the chloritized basalt unit  
111 that underlies the silicified wallrock breccia zone, as the drillholes did not intersect the interface  
112 between chloritized and unaltered basalt. Additionally, to estimate the mound's sulfide mineral  
113 tonnage, symmetry was assumed orthogonal to the 2D geologic interpretation (Hannington et al.,  
114 1998). This study expands on our previous knowledge of the geometry of seafloor SMS  
115 hydrothermal alteration units by inverting for a 3D geophysical model of the chloritized basalt  
116 unit, as well as a 3D model of the deposit.

117 The two most commonly used methods for modelling magnetic data from SMS deposits are  
118 those of Parker & Huestis (1974) and Honsho et al. (2012), which both solve for two-  
119 dimensional volume magnetization distributions. The distribution varies laterally, with no  
120 vertical changes and a fixed thickness to the magnetized crustal layer, typically 500 m (Szitkar &  
121 Dyment, 2015), but the thickness has also been defined by the Curie isotherm depth (Bouligand  
122 et al., 2020). Minimum-structure inverse modelling can be an effective alternative method to  
123 model the variations in physical properties around and within SMS deposits (Kowalczyk, 2011;  
124 Caratori Tontini et al., 2012; Galley, et al., 2020a). This modelling method uses a three-  
125 dimensional discretization of the crust, known as a mesh, and solves for the target physical

126 property values inside each of the mesh's cells. Minimum-structure inverse modelling is robust,  
127 requiring little prior knowledge of the subsurface to construct a feasible geophysical model  
128 (Constable et al., 1987). Here, the minimum-structure inverse modelling uses the method as  
129 described in Galley et al. (2020a), which discretizes the crust using a tetrahedral mesh as to  
130 closely fit the variable bathymetry and solves for the effective magnetic susceptibility in each  
131 tetrahedral cell.

132 Minimum-structure inverse models are smooth by design and as such can have difficulty  
133 determining the locations of discrete or almost discrete boundaries between petrophysically  
134 contrasting lithological units. To further improve upon a subsurface physical property model, a  
135 surface geometry inversion (SGI) method can be used to solve for a wireframe model of an SMS  
136 deposit (Galley et al., 2020b). Our SGI method creates a wireframe surface model of rock unit  
137 contacts by inverting for the 3D position of the vertices that define the surface mesh. This is  
138 accomplished using first a Genetic Algorithm (GA) to find the model that best fits the data,  
139 followed by a Monte-Carlo Markov chain (MCMC) seeded with the GA's inversion model to  
140 calculate the model's uncertainty. Modelling SMS deposits as wireframe models creates  
141 geophysical models that are formatted similar to geological interpretations and allow for the  
142 volumes of alteration units to be easily calculated.

143 Previous geophysical models of the TAG active mound have included inverting magnetic data to  
144 study the lateral variations in magnetization at the deposit (Szitkar & Dymont, 2015; Tivey et al.,  
145 1993), as well as inverting controlled-source electromagnetic (CSEM) data to develop 2D  
146 conductivity cross-sections through the TAG mound (Gehrmann et al., 2019). The magnetization  
147 models have led to the lateral extents of the near-surface hydrothermal alteration to be mapped,  
148 allowing the deposit to be identified by a low magnetization model feature that extends into the  
149 seafloor; however the models did not identify the vertical variations in the deposit's alteration.  
150 Gehrmann et al. (2019)'s CSEM inversions included two ~100 m thick cross-sectional models  
151 that passed orthogonally through the TAG active mound, allowing the high conductivity regions  
152 associated with massive sulfide mineralization to be identified. The relatively shallow depth of  
153 penetration of these CSEM models allows them to map the conductivity anomalies in the upper  
154 alteration units of the mound, but the smooth nature of the minimum-structure inversion models

155 limits the model resolution and creates difficulties when trying to identify the thickness of the  
156 zone of mineralization.

157 With the incorporation of the Leg 158 drilling information, AUV magnetic data collected during  
158 the 2016 RV Meteor M127 cruise (Petersen and Shipboard Scientific Party, 2016) and seafloor  
159 gravity data collected in the Shinkai 6500 submersible (Evans, 1996), magnetic minimum-  
160 structure along with magnetic and gravity SGI models are used to develop a new three-  
161 dimensional geological model of the TAG active mound system. This model relies on two steps:  
162 1) modelling of the effective magnetic susceptibility distribution around and within the TAG  
163 active mound using minimum-structure inverse modelling; 2) modelling the discrete contact  
164 boundaries between the deposit and surrounding basalt host rock using magnetic and gravity  
165 SGI. The region of low effective magnetic susceptibility in the magnetic inversions models the  
166 extent of the chloritized basalt unit, and the gravity inverse modelling solves for the geometry of  
167 the massive sulfide layer. Our modelling has developed, to the best of our knowledge, the first  
168 3D model of the TAG mound derived from geophysical data, an improved sulfide tonnage  
169 estimate evaluation for the deposit, and a better understanding of the deposit-scale hydrothermal  
170 fluid circulation.

171

## 172 **2 Methods**

173 Two modelling methods were used in this study, the minimum-structure inverse modelling  
174 method and the surface geometry inversion method. Both solve for the form of a spatial  
175 distribution of a physical property in the crust but do so in two fundamentally different ways.

### 176 **2.1 Minimum-structure Inverse Modelling**

177 The minimum-structure inversion method is arguably the most common inverse modelling  
178 method used in geophysical studies (Farquharson & Lelièvre, 2017), which we used on the  
179 magnetic data. The method solves for a smooth distribution of the target physical property in the  
180 subsurface, generating a blurred subsurface model. A cell-based mesh is used during minimum-  
181 structure inversions, which discretizes the subsurface into many fixed voxels that each contain a  
182 homogeneous physical property value. In our minimum-structure magnetic modelling we use a

183 tetrahedral discretization for all the inversions' meshes, as these unstructured meshes allow for  
 184 very accurate representation of variable bathymetry on the surface of the mesh as well as being  
 185 able to efficiently incorporate zones of variable mesh discretization (Lelièvre et al., 2012). To  
 186 construct our meshes we use the program *Triangle* (Shewchuk, 1996) to develop a 2D Delaunay  
 187 triangular surface to represent the bathymetric surface, and the program *Tetgen* (Si, 2015) to fill  
 188 the 3D volume below the bathymetric surface with tetrahedra.

189 The minimum-structure inversion approach used here considers an objective function structured  
 190 as,

$$\boldsymbol{\phi} = \lambda \boldsymbol{\phi}_d + \boldsymbol{\phi}_m, \quad 1$$

191 with an L2 norm data misfit

$$\boldsymbol{\phi}_d = \frac{1}{N} \sum_{i=1}^N \frac{(\mathbf{d}_{i,pred} - \mathbf{d}_{i,obs})^2}{\sigma_i^2} \quad 2$$

192 and model measure  $\boldsymbol{\phi}_m$ .  $\lambda$  is the trade-off parameter between the data and model measure  
 193 (Constable et al., 1987). The predicted data,  $\mathbf{d}_{i,pred}$ , are calculated using Okabe (1979)'s  
 194 algorithm, the observed data,  $\mathbf{d}_{i,obs}$ , are the measured magnetic data with noise  $\sigma_i$ . The model  
 195 measure only contains a smoothing term, as no smallness measure or reference model was used  
 196 in the inverse modelling,

$$\boldsymbol{\phi}_m = \mathbf{v}_f^T \mathbf{W}_s (\mathbf{D}_f \mathbf{m})^2. \quad 3$$

197 In Eq. 3  $\mathbf{W}_s$  is the weighting matrix,  $\mathbf{v}_f$  the array of integration cell volumes, and  $\mathbf{D}_f$  is the  
 198 general difference matrix applied to the array of model parameters  $\mathbf{m}$  (Lelièvre & Farquharson,  
 199 2013). In Eq. 3 the L2 norm is used on the model misfit (Constable et al., 1987), as well as a

200 variation of Li & Oldenburg (2000) sensitivity weighting, to preferentially weight cells with low  
 201 sensitivities, whose array is composed of elements

$$w_j = \left( \sum_{i=1}^N \left| \frac{G_{ij}}{v_j} \right|^2 \right)^{1/2}, \quad 4$$

202 for the  $j^{th}$  cell in the mesh with  $N$  cells, whose volume is  $v_j$ .  $\mathbf{G}$  denotes the inverse problem's  
 203 sensitivity matrix, with elements  $G_{ij}$ .

204 A magnetic susceptibility minimum-structure inversion is sufficient to resolve an accurate  
 205 magnetic Earth model when there is negligible remanent magnetization present in the region of  
 206 study, or when the remanent magnetization present is parallel with the Earth's inducing field  
 207 vector. If significant remanent magnetization oblique to the Earth's inducing field is present then  
 208 simply solving for a magnetic susceptibility will create an incomplete and likely incorrect Earth  
 209 model, requiring a total magnetic vector inversion (TMVI) to be used instead (Lelièvre &  
 210 Oldenburg, 2009). A TMVI solves for the magnetization vector in each of the model's cells,  
 211 parameterized in the 3D Cartesian or spherical coordinate systems. For greater control on  
 212 constraining the magnetization's inclination and declination, the spherical system can be used  
 213 resulting in a model objective function of

$$\Phi_m = \|\mathbf{W}_r(\mathbf{r} - \mathbf{r}_{ref})\|^2 + \gamma \|\mathbf{W}_\varphi(\varphi - \varphi_{ref})\|^2 + \gamma \|\mathbf{W}_\theta(\theta - \theta_{ref})\|^2, \quad 5$$

214 being used where  $\mathbf{W}_r$ ,  $\mathbf{W}_\varphi$ , and  $\mathbf{W}_\theta$  are the smoothness terms for the magnitude,  $\mathbf{r}$ , inclination,  
 215  $\varphi$ , and declination,  $\theta$ , of the magnetization vector, respectively.  $\mathbf{r}_{ref}$ ,  $\varphi_{ref}$ , and  $\theta_{ref}$  correspond  
 216 to the reference model parameters and  $\gamma$  is a weighting parameter typically set to  $10^{-3}$  (Lelièvre &  
 217 Oldenburg, 2009).

218

## 219 **2.2 Regional Removal**

220 A regionally-removed process can be applied to a dataset to remove the signal of regional  
 221 features about some defined volume of interest, allowing the inverted regionally-removed data to

222 produce a physical property distribution of solely within the volume of interest. The process  
223 begins by creating an inversion model that overfitted the observed data (e.g. assuming a 0.3%  
224 noise). Overfitting the data is important during this step as it ensures there is no loss of signal  
225 amplitude from the data that represents a physical property distribution within the volume of  
226 interest. The cells within the over-fitted inversion model's volume of interest are then removed,  
227 and the forward signal of the remaining regional cells is calculated. Subtracting this forward  
228 signal from the observed data set results in the regionally-removed data set (see Fig. S5 for the  
229 workflow; Li & Oldenburg, 1998). The regionally-removed data can then down-sampled as the  
230 outer data points would be no longer necessary to depict the volume of interest's magnetic  
231 response.

232

### 233 **2.3 Surface Geometry Inverse Modelling**

234 The second inversion method used in this study is the SGI method of Galley et al., (2020b),  
235 which was used on both the magnetic and gravity data. Rather than solving for the physical  
236 properties in several cells, the SGI method holds the physical property values in a number of  
237 geometry bodies constant and alters the shape of the body until the predicted data sufficiently fit  
238 the observed geophysical data. Each of these anomalous bodies are parameterized by a surface  
239 tessellation of triangular facets, defining the discrete contact between differing geologic units. As  
240 such, the inversion method is parameterized by the 3D Cartesian coordinates of each vertex that  
241 defines the wireframe surface mesh. This parameterization often leaves the inverse problem  
242 over-determined, reducing the non-uniqueness of the problem compared to the under-determined  
243 minimum-structure method. Okabe (1979)'s forward algorithm was also used by this inversion  
244 program.

245 The topology of the SGI's wireframe surface mesh is not able to vary throughout the inversion,  
246 and as such its initial design holds some weight on how close of a data fit will be possible. The  
247 initial models used in this study were created from contact boundaries observed in the drillcore.  
248 To construct the wireframe surface meshes the program *FacetModeller* was used (Lelièvre et al.,  
249 2018), which allowed the user to place the defining vertices in 3D space and govern their  
250 connectivity through manual placement of the surface's triangular facets. As such, it is simple to

251 incorporate any prior geologic information in the surface mesh, such as location of lithological  
252 contacts derived from borehole samples. However, the discretization of the surface mesh is  
253 altered during the SGI by applying a cubic B-spline to the models prior to calculating their  
254 forward responses, allowing few “control nodes” defined as the vertices from the initial model to  
255 represent a finer surface mesh (see Galley et al., 2020b for more details).

256 A GA was used to minimize the inversion’s objective function, which is simply the data misfit,  
257 as the method’s spatial parameterization has the possibility to add local minima to the solution  
258 space. After a best fit model is found from the GA a MCMC sampling is used to derive a model  
259 uncertainty and a mean inversion model. The MCMC uses the Metropolis-Hastings algorithm  
260 with a single chain, sampling different positions of the model’s vertices over 1 million iterations.

261 An assumption that has been made in the developed SGI method's design is that the physical  
262 properties of each rock unit in the model remained fixed during the inversion. It is trivial to allow  
263 those physical properties to change as well as the surface geometry parameters (control node  
264 coordinates) by adding the physical properties of each homogeneous model region to the model  
265 parameter vector. Instead, a suite of inversion models was produced with different physical  
266 property values, and these models were accessed relative to the drilling information to determine  
267 the best model.

268

## 269 **3 Data**

### 270 **3.1 Bathymetric Data**

271 The bathymetric data were collected during the 2016 R/V Meteor M127 cruise using GEOMAR  
272 AUV *Abyss*, equipped with a RESON Seabat 7125 multibeam echosounder. The echosounder  
273 used a frequency of 200 kHz. The surveys were flown at a speed of 3 knots, a line spacing of 80-  
274 100 m, and an average altitude of 84 m relative to the seafloor, resulting in a 2 m resolution  
275 bathymetric data set (Petersen and Shipboard Scientific Party, 2016). The bathymetric data was  
276 merged using the software package MB Systems based on the location of prominent seafloor  
277 features, including the re-entry cone placed on the TAG mound during the 1994 ODP drilling  
278 that was visible in the high-resolution data. Erroneous soundings were removed using QPS

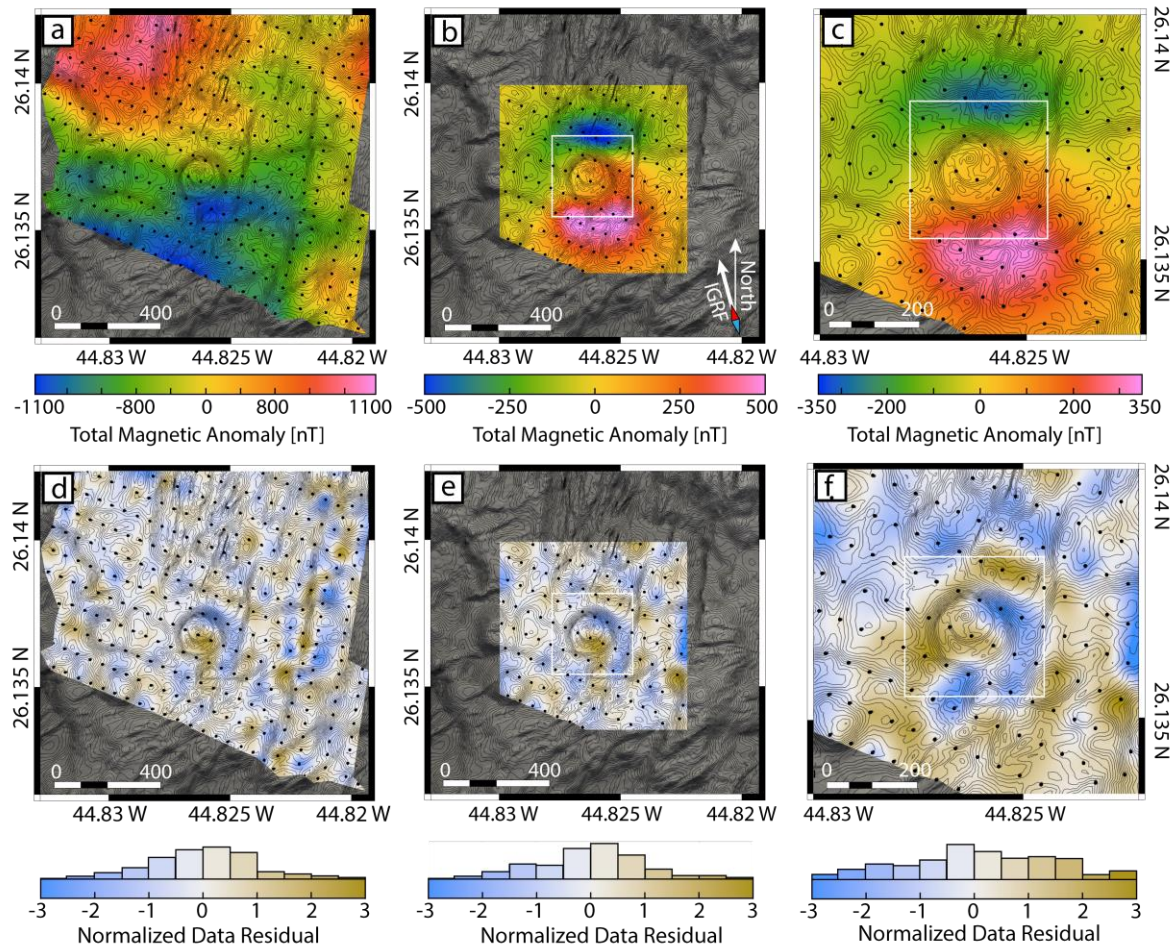
279 Qimera. From the original dataset a 3 by 3 km<sup>2</sup> region centered on the TAG active mound was  
280 used in this study (Fig. 1a).

### 281 **3.2 Magnetic Data**

282 During the M127 cruise, *Abyss* was equipped with an Applied Physics System APS 1540 Digital  
283 3-Axis Miniature Fluxgate Magnetometer, which collected measurements at a 10 Hz sampling  
284 rate along the same grid as the bathymetry data. During the cruise the Earth's inducing field  
285 vector had an inclination of 42°, declination of -15°, and field strength of 38,290 nT. The  
286 magnetic data set was cropped to only include measurements within the 1.2x1.2 km<sup>2</sup> region  
287 centered on the TAG active mound (Fig. 2a). The magnetic dataset was processed to remove the  
288 induced and permanent magnetization effects from the AUV by conducting a figure-eight  
289 calibration dive with the AUV/magnetometer and using those data to solve for the AUV's  
290 magnetic properties with a least-squares method (Honscho et al., 2013). The magnetic data were  
291 also low-pass filtered with a 0.25 Hz cut-off to remove very short wavelength features associated  
292 with noise and the effects of the AUV propeller. The dataset was then down-sampled to a point  
293 every 50 m along the survey lines to reduce the computational expense of the inverse modelling,  
294 without reduction in the quality of the constructed models. The 50 m down-sampling was done

295 while not producing any aliasing artifacts resulting from sampling at a distance greater than half  
 296 the wavelength of the magnetic waveforms.

297



298

299 **Figure 2.** Processed data used in the magnetic inverse modelling. **a)** The total magnetic anomaly  
 300 data measured during the RV Meteor M127 cruise, used in the regional minimum-structure  
 301 inverse modelling; **b)** the regional-removed magnetic anomaly data used in the deposit-scale  
 302 minimum-structure inverse modelling; **c)** the regional-removed and filtered magnetic anomaly  
 303 data used in the SGI; and **d-f)** are the respective normalized data residuals form the inversions of  
 304 the data in **a-c)**. In **b, c, e,** and **f)** the white outline represents the extent of the deposit-scale mesh.

305 In all images the locations of the observation points are shown as black dots and 5 m bathymetric  
 306 contour lines are shown in black.

307

308 The magnetic data's noise is an unknown in this study. The magnetometer has very low system  
 309 noise (quantified at 0.5 nT), but the uncertainty in the observation points' lateral positions creates  
 310 a larger, secondary noise. In comparison, the vertical position of the AUV, determined from  
 311 altimeter and depth readings collected while surveying, is more precise. The AUV's lateral  
 312 position is tracked from an initial calibrated position using an inertial navigation system. Ideally,  
 313 this would be able to accurately locate the position of the AUV throughout its surveying, but any  
 314 seafloor currents will gradually shift it away from its inferred position. An 8% relative noise was  
 315 assigned to the data, derived by adjusting how closely the study's minimum-structure inversion  
 316 models could fit the data without producing artifacts. This noise would be equivalent to a 6-8 m  
 317 uncertainty in the AUV's lateral position (Fig. S1).

### 318 **3.3 Gravity Data**

319 The dataset from the gravity survey collected over the TAG active mound was composed of 11  
 320 stations roughly aligned along a North-South line crossing the mound (Fig. 3a, b), collected  
 321 during the 1994 R/V Yokosuka MODE'94 cruise. The measurements were collected manually  
 322 from within the Shinkai 6500 submersible on the seafloor with a Scintrex CG-3 autograv  
 323 gravimeter (Evans, 1996). The data were first levelled using the northern most station as a  
 324 reference point, then processed to develop the free-water anomaly,

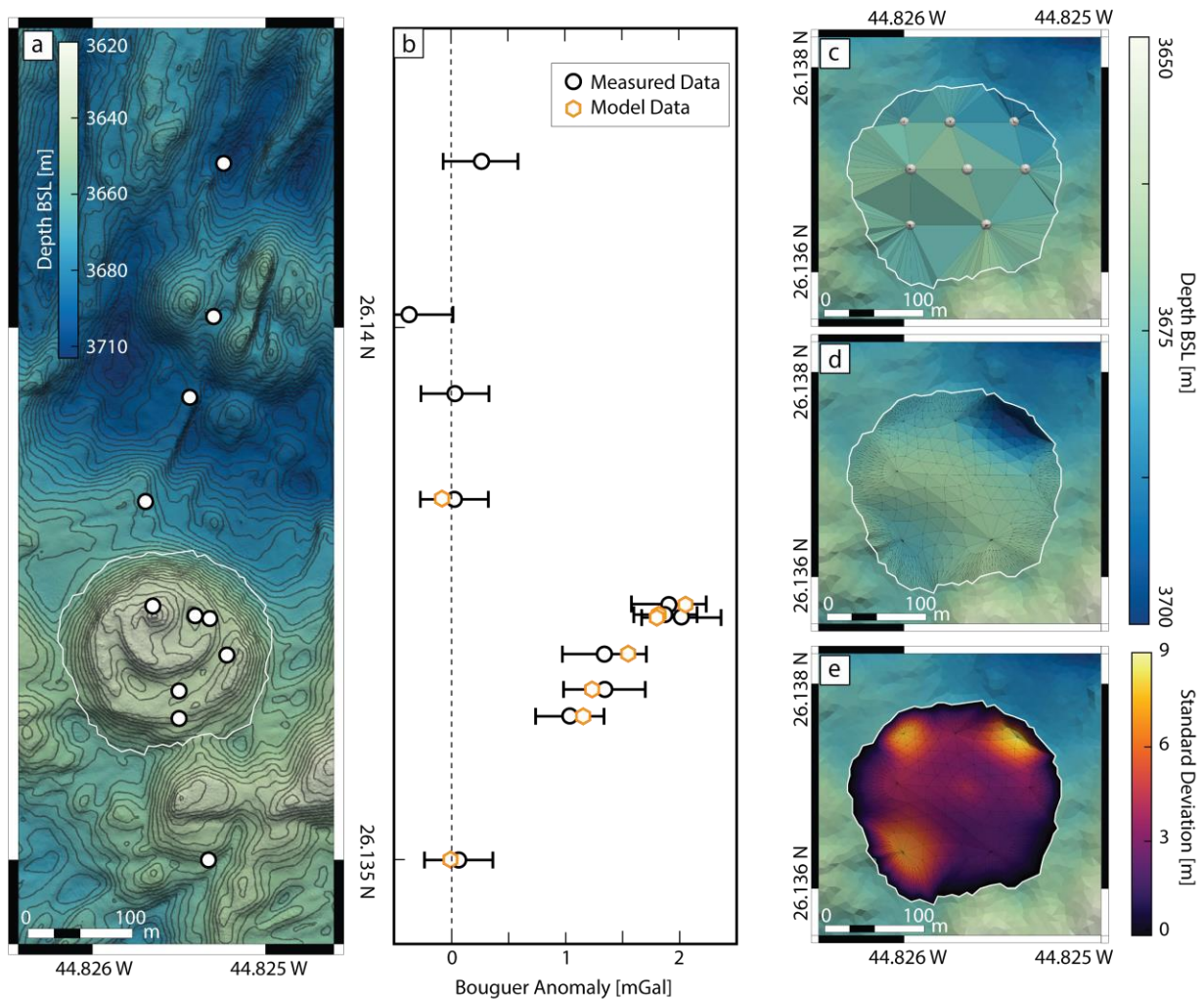
$$\begin{aligned} g_F &= (\gamma_a - 4\pi\rho_w G)D \\ &= \mathbf{0.222D} \end{aligned}$$

6

325 where  $\gamma_a = 0.309$  mGal/m is the free-air gradient,  $\rho_w = 1.02$  g/cm<sup>3</sup> was used as the density of  
 326 seawater,  $G$  is the gravitational constant, and  $D$  is the array of station elevation measurements  
 327 relative to the reference station (Ishihara et al., 2018). The forward signal of a background model  
 328 built with 2 m resolution bathymetric data of the seafloor about the mound, with density 2.4

329  $\text{g}/\text{cm}^3$  (Evans, 1996), was then removed to produce the Bouguer anomaly data. The 2 m  
 330 resolution bathymetric data did not extend sufficiently far away from the observation points, so  
 331 the linear trend left in the Bouguer anomaly data was calculated with a least-squares method and  
 332 removed. The gravity data's noise was derived from the system noise of the gravimeter, as well  
 333 as the compounding uncertainties associated with the data processing.

334



335

336 **Figure 3.** The gravity data collected over the TAG active mound as well as its SGI model. **a)**  
 337 The locations of the gravity measurement stations are shown on the bathymetric map; **b)** a plot  
 338 displaying the measured Bouguer anomaly data (black circles) compared to the data resulting  
 339 from the SGI (orange hexagons); **c)** the initial model for the base of the massive sulfide layer

340 shown relative to the surrounding bathymetry; **d**) the SGI result relative to the surrounding  
341 bathymetry; and **e**) the SGI model colored based on the standard deviation of the vertical  
342 position of the surface model. The black contour lines in **a** mark 5 m depth intervals and the error  
343 bars in **b** signify the magnitude of the data's standard deviation.

344

## 345 **4 Results**

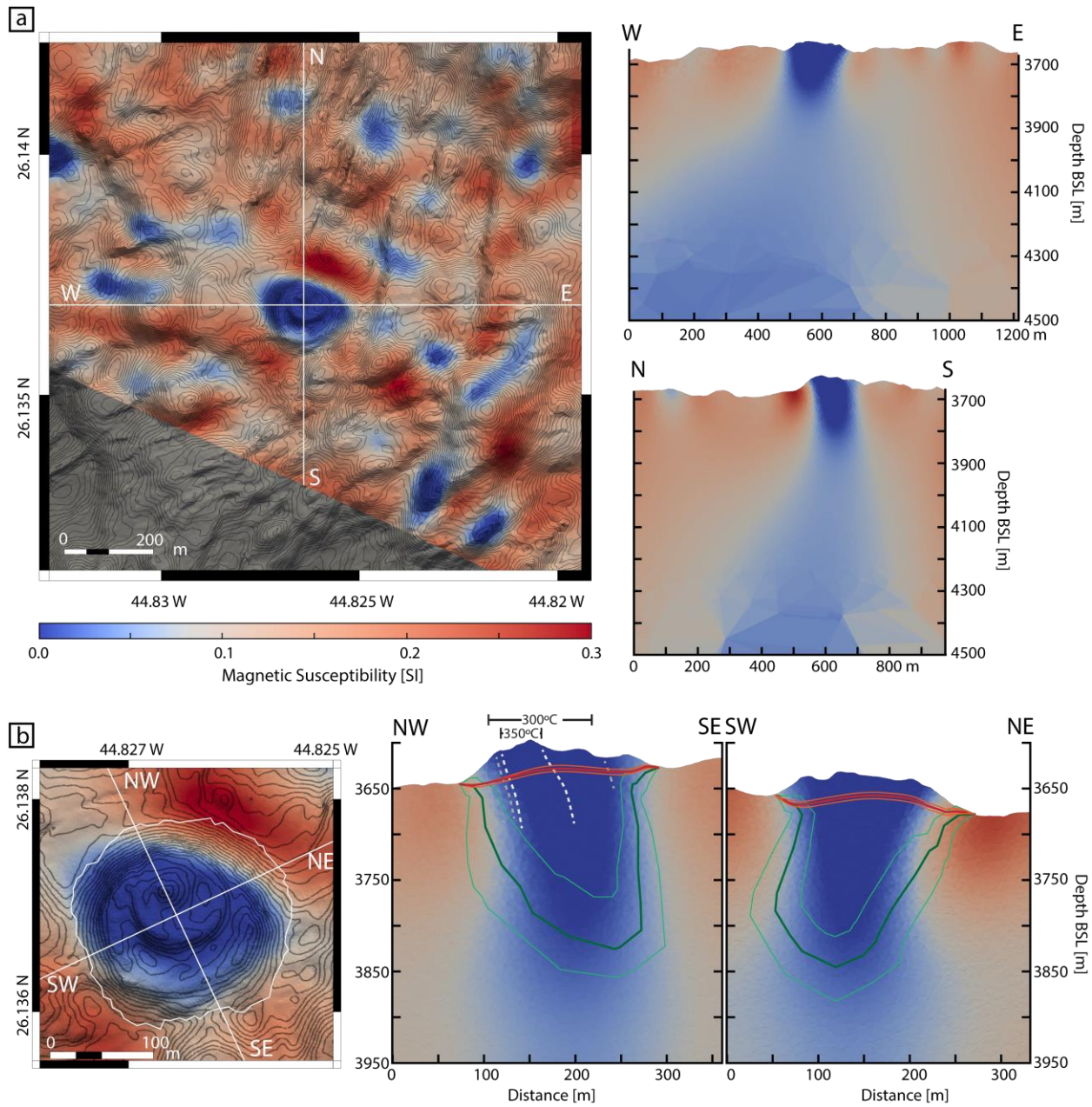
### 346 **4.1 Magnetic Inverse Modelling**

347 Firstly, a TMVI model was constructed to assess the amount of remanent magnetization in the  
348 crust surrounding the TAG active mound (Fig. S3), which was used to conclude that there was  
349 no significant remanence present (this is discussed in greater detail in Section 5.2). Therefore,  
350 scalar magnetic susceptibility inversions were sufficient for this study. Two magnetic  
351 susceptibility minimum-structure inversion models were then constructed to produce first-pass  
352 three-dimensional magnetic susceptibility distributions that fit the observed data (Fig. 2a).  
353 Firstly, a regional minimum-structure model was produced (Fig. 4a), from which we could  
354 determine the volume of seafloor that fully encompasses the magnetic low representing the  
355 hydrothermal alteration associated with the deposit. The larger scale, scalar magnetic inversion  
356 was solely used to determine the minimum volume of altered oceanic crust around the TAG  
357 mound, so that more detailed inversion models could be constructed and studied (Fig. 4b).

358 To perform small-scale modelling of the deposit, a regional data removal was used to isolate a  
359 300 by 300 by 300 m<sup>3</sup> volume enclosing the mound (see Section 2.2; Li & Oldenburg, 1998).  
360 Comparing the magnetic features between the regional and deposit-scale inversion models  
361 affirms that the regional-removal did not subtract any data features that correspond to magnetic  
362 features in the isolated volume (Fig. 4). Both minimum-structure inversions used a positivity  
363 constraint on their effective magnetic susceptibility. The regional inversion took 25 iterations

364 and 4.1 hours to complete, and the deposit-scale inversion took 24 iterations and 45 minutes.  
 365 Each inversion was run in parallel on 48 threads on a 2.20 GHz Intel Xeon E5-2650 Processor.

366



367

368 **Figure 4.** The minimum-structure inversion results from the regional and deposit-scale models.  
 369 **a)** The regional model shown in plan view and West-East and North-South cross sections. **b)** The  
 370 deposit scale minimum-structure model. The mean surface-intersect for the chloritized basalt

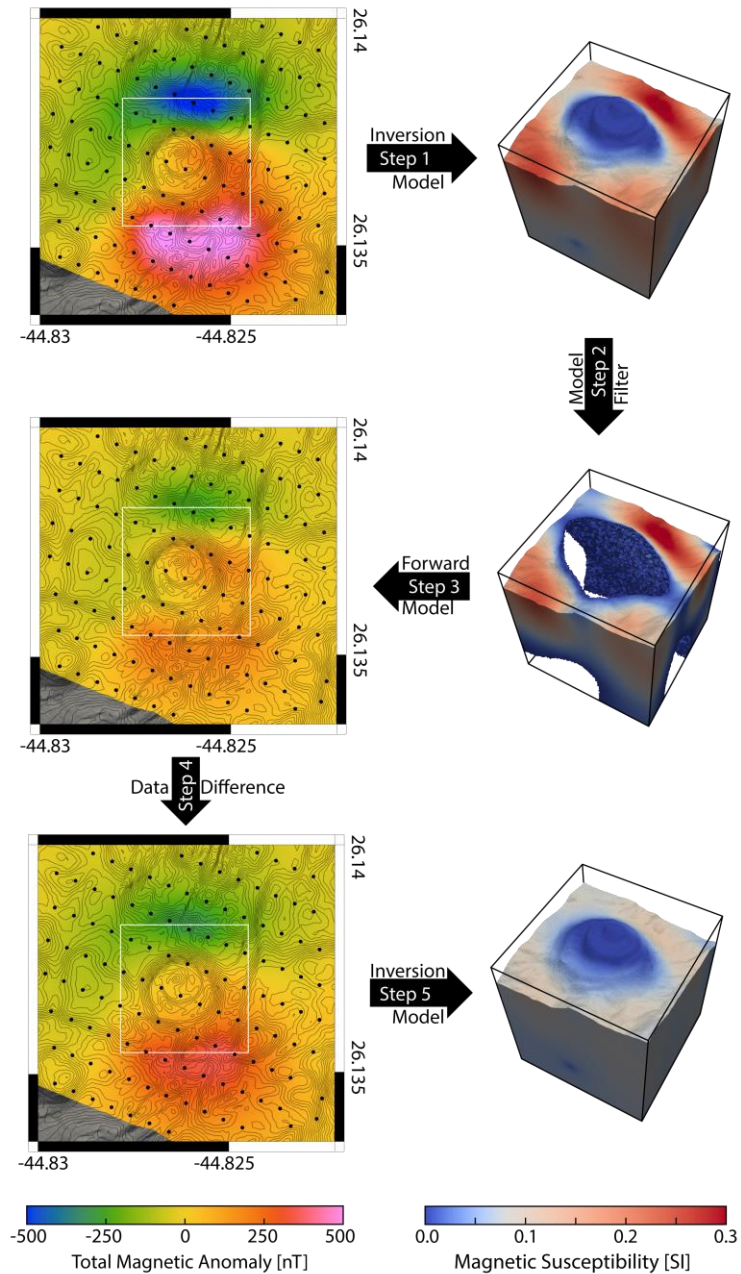
371 SGI is shown as a dark green line, and the base of the massive sulfide SGI layer in red. The one  
372 standard deviation shifted models are shown as a light green line for the chloritized basalt model,  
373 and orange for the massive sulfide model. Bathymetric contour lines (5 m interval) are shown in  
374 black. In the deposit-scale cross sections, **b**, isotherms are overlain onto the bathymetry to  
375 compare with the geometry of the magnetic low anomaly (Grant et al., 2018).

376

377 Next, we applied an additional processing procedure to further refine the magnetic data near the  
378 TAG active mound in preparation for the more targeted SGI modelling. Ideally, when  
379 constructing surface models of the subsurface one would want a homogeneous background with  
380 the single anomalous body contained within. However, the crust directly adjacent to the TAG  
381 active mound is inhomogeneous, containing zones of anomalously high magnetic susceptibility  
382 near the seafloor likely indicating areas of younger extrusive rocks (Fig. 4b). To remove the  
383 components of the magnetic data that correspond to the anomalously high regions, a five step  
384 workflow was developed (Fig. 5): 1) invert the data derived from the regional removal; 2) isolate  
385 the cells that contain magnetic susceptibilities above the observed background value in the  
386 regional inversion model (in this case 0.08 SI; Fig. 4b), subtract the background value from the  
387 magnetic susceptibilities in the isolated cells to get anomalous susceptibilities relative to the  
388 background (0.08 SI); 3) calculate the forward signal from the isolated cells derived from step 2;  
389 4) subtract the isolated cells' forward signal from the regional-removed data; and 5) invert the

390 resulting data set to create a magnetic susceptibility model effectively free of anomalously high  
 391 magnetic susceptibility regions.

392

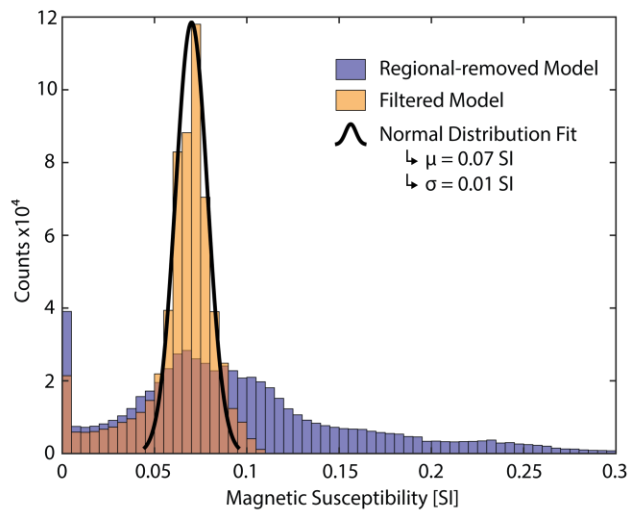


393

394 **Figure 5.** The workflow to deprivate the magnetic data from undesirable anomalously high  
 395 magnetically susceptible regions of a voxel inversion model.

396

397 The background value of 0.08 SI was chosen from the distribution of magnetic susceptibilities in  
 398 the regional-removed model. As seen in Figure 6, there are 2 major peaks in the histograms, one  
 399 about 0.0 SI representing the anomalously low magnetic susceptibility of the TAG active mound,  
 400 and the second at 0.08 SI representing the background. The curve representing the model's  
 401 background magnetic susceptibility in the regional-removed model is wider compared to the  
 402 filtered model. After further processing the data by removing the signal components related to  
 403 the high magnetic susceptibility region (Fig. 5), the filtered model distribution develops a more  
 404 prominent mean at 0.07-0.075 SI bin (Fig. 6). Fitting a normal distribution to the background  
 405 susceptibility values in the filtered model results in an approximate distribution with mean 0.07  
 406 SI and 0.01 SI standard deviation.



407

408 **Figure 6.** Two histograms representing the distribution of magnetic susceptibility values in the  
 409 cells of the region-removed and 0.08 SI filtered models.

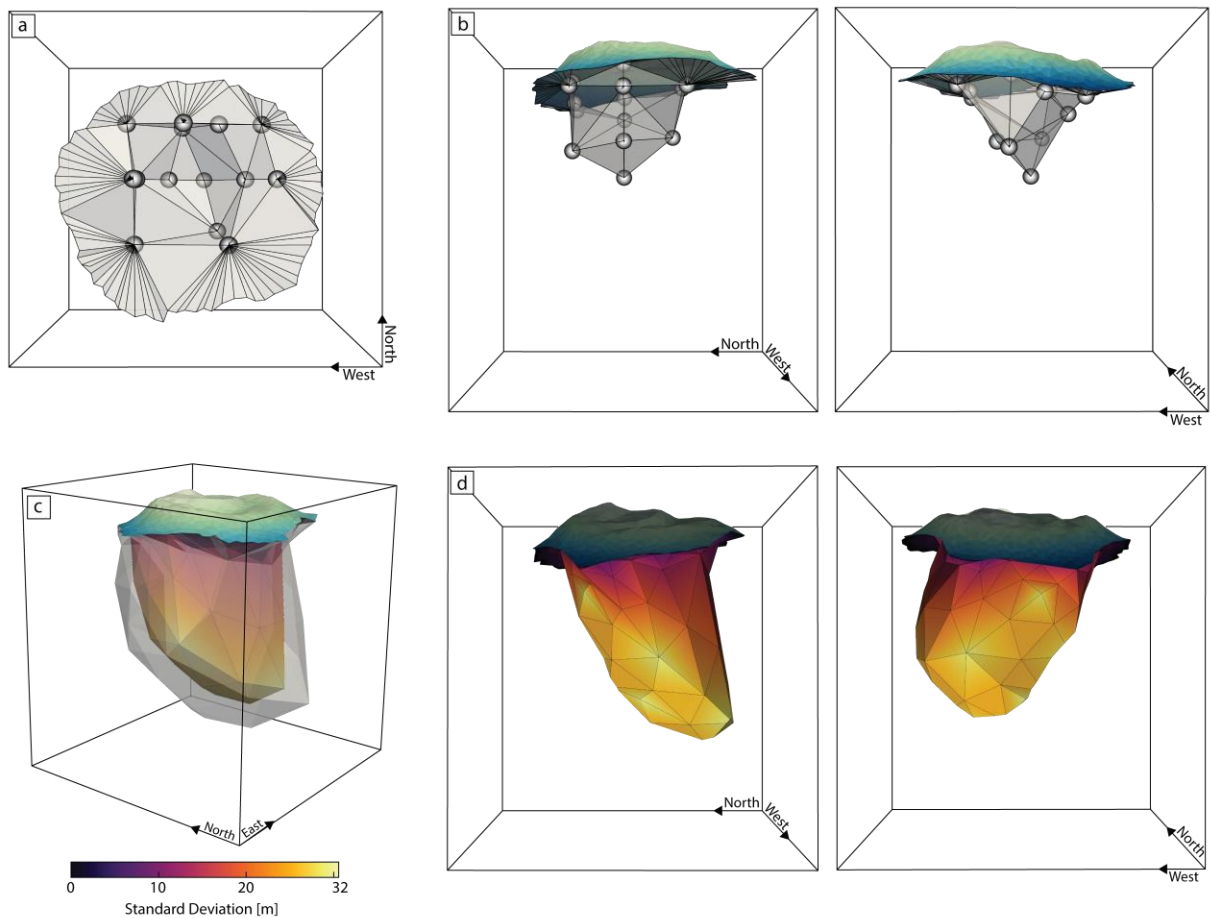
410 An SGI can now be performed on the resulting filtered data (Fig. 2c) to model the TAG active  
 411 mound as an anomalous low inside an approximately homogeneous background. The first step in  
 412 our SGI is to design an initial model for the inversion. Spatial bounds are then applied to the  
 413 model vertices to develop an initialization volume. The initialization volume is defined as the  
 414 volume of space that the solution model is assumed to exist in and acts as the search volume

415 during the inversion process. For the TAG active mound, the drillcore provide enough  
416 information to develop an initial model.

417 The initial model for the chloritized basalt (Fig. 7a, b) was defined as the inferred inner surface  
418 of this alteration type (see Fig. 1b for the drilling information), acting as a minimum volume that  
419 the SGI would then expand. The surface model was composed of 14 vertices, each of which  
420 could move in all three dimensions, resulting in 42 inversion parameters for the SGI. We held the  
421 model's physical properties constant throughout the inversion, using a value of  $10^{-5}$  SI for the  
422 TAG active mound (Zhao et al., 1998), and a value of 0.08 SI for the background, as derived  
423 from the voxel inverse modelling. To bound the vertices in 3D, relative to their initial position  
424 (see Fig. 7a, b), constraints were assigned: +/- 30 m for the upper seven vertices in the horizontal

425 (East-West and North-South) plane, and vertical constraint of +0 m/-20 m; +/- 100 m  
 426 horizontally for the lower seven vertices, and +20 m/-300 m vertically.

427



428

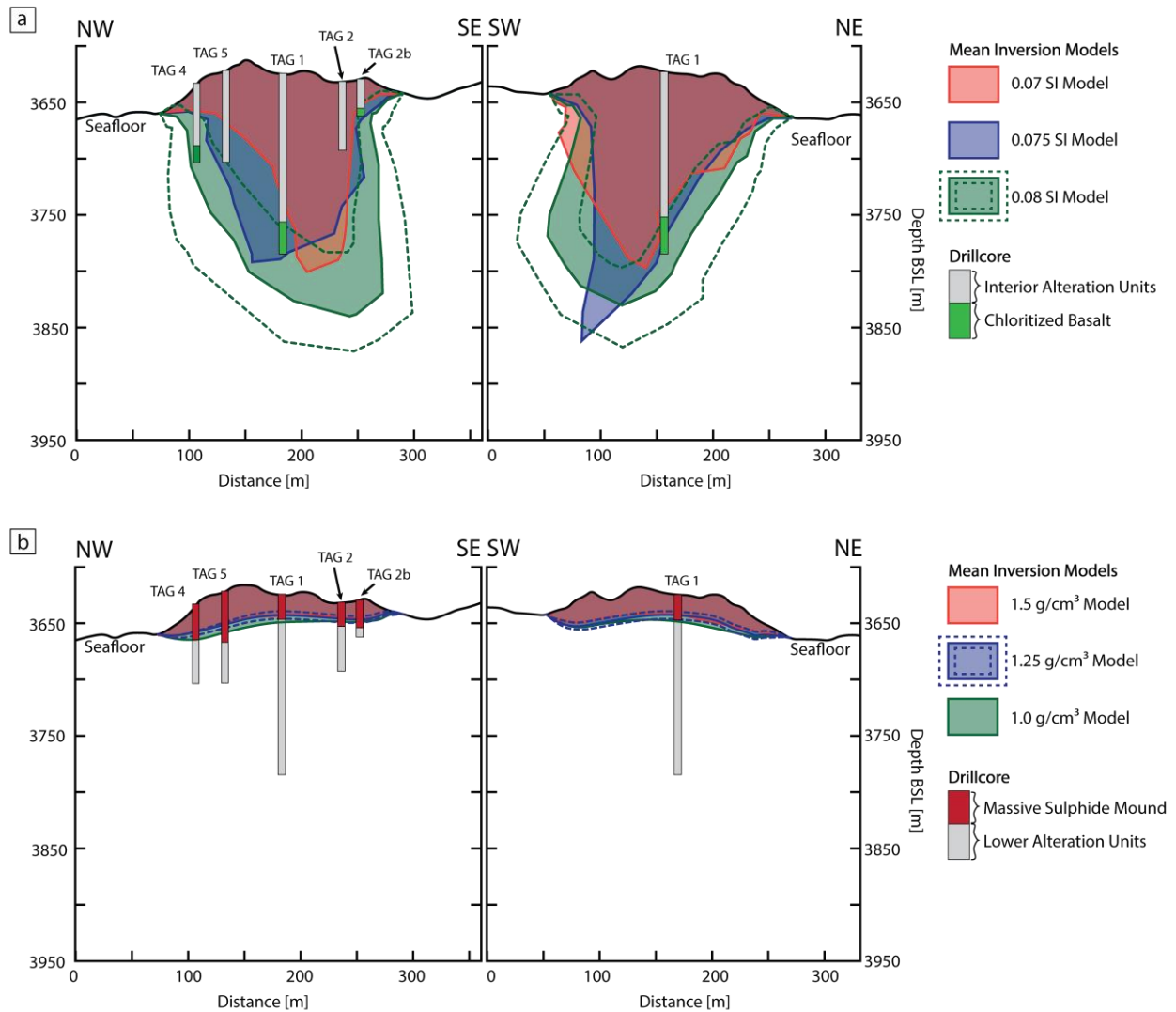
429 **Figure 7.** The initial model **a, b** and inversion result **c, d** for the magnetic SGI. **a)** The plan view  
 430 of the initial magnetic model with the bathymetry surface of TAG removed, and **b)** the same  
 431 model including the bathymetric surface side on. The vertices of the initial model are grey  
 432 spheres, and the top of the TAG active mound is colored based on its bathymetry. **c)** The TAG  
 433 active mound's sub-seafloor hydrothermal alteration SGI model result, with the mean model  
 434 colored based off its vertices' standard deviations. The translucent grey surface is the mean

435 model expanded by one standard deviation. **d)** Two half-slices of the magnetic and gravity SGI  
436 models, colored by the surfaces' vertices' standard deviations.

437

438 As the physical properties in the SGI model are constant throughout the modelling, some  
439 uncertainty assessment is required to justify the choice of the anomalous and background  
440 susceptibilities. The assessment was performed by creating a suite of SGI models with different  
441 magnetic susceptibility values, comparing the different models to the active mound's drillcore,  
442 then choosing the most geologically accurate model. The range of background magnetic  
443 susceptibilities were chosen from the fitted normal distribution of Fig. 6, which had a mean of  
444 0.07 SI and a standard deviation of 0.01 SI, created a range of [0.06, 0.08] SI. SGI models  
445 created with background susceptibilities of less and or equal to 0.075 SI produced a chloritized  
446 basalt model that was too small and did not agree with the bounds on the alteration units as  
447 defined from the drillcore. Models inverted with background values of 0.07, 0.075, and 0.08 SI  
448 (Fig. 8a) demonstrating the change in model geometry that results from using different magnetic

449 susceptibility values. Within the  $0.07 \pm 0.01$  SI range the background value of 0.08 SI produced  
 450 the best model, agreeing most with the drillcore.



451

452 **Figure 8.** A comparison on the geometry of **a)** the magnetic SGI model inverted with three  
 453 different background magnetic susceptibility values: 0.07, 0.075, and 0.08 SI, and **b)** the gravity  
 454 model with anomalous mound densities of 1.0, 1.25, and 1.5 g/cm<sup>3</sup>. The anomalous density being  
 455 the contrast between the massive sulfide mound's density and the background basalt's density.  
 456 Each of the 3D models are shown as two cross-sections, the left cross-section running parallel to  
 457 the drillcores, and the right-hand cross-section perpendicular to it, following the same

458 orientations as in Fig. 4b. In **a** and **b** the dotted lines represent a one standard deviation  
459 uncertainty on the position of the model's vertices.

460

461 The SGI for the chloritized basalt model took 90 seconds to complete the GA optimization, and  
462 5.5 hours to complete the MCMC sampling (see Fig. S2 for the convergence curves). Both  
463 programs were run on 48 threads on a 2.20 GHz Intel Xeon E5-2650 Processor, with the GA  
464 running in parallel and the MCMC in serial. The result of the magnetic SGI is shown in Figure  
465 4b compared to the magnetic voxel inversion model, and again in Fig. 7c, d.

466 For both magnetic and gravity SGI modelling the number of vertices chosen to define the initial  
467 model were defined such that each problem would be over-determined. Treating this requirement  
468 as an upper bound to the initial model's vertices count, the vertices were then reduced such that a  
469 minimum number were used without loss of model features.

#### 470 **4.2 Gravity Inverse Modelling**

471 As the gravity data only consisted of 11 stations, all roughly along a north-south line, a  
472 minimum-structure inversion of the data would be poorly constrained and produce an ambiguous  
473 subsurface model. Therefore, only SGI models were created from the gravity data. Of the eleven  
474 stations, only the eight closest to the TAG mound were used to develop the SGI model as the  
475 other three had low signal sensitivity to the density of the TAG mound.

476 The initial model for the base of the massive sulfide layer (Fig. 3c) was derived from the  
477 available drillcore data. The vertices for the gravity SGI were constrained with +10 m/-50 m  
478 bounds relative to the starting model solely in the vertical direction, as the model for the massive  
479 sulfide was already well constrained from the drilling. Additionally, as the gravity data was  
480 organized in an approximate North-South line any East-West variations in the vertices' positions  
481 could not be constrained. Density values of 3.65 g/cm<sup>3</sup> and 2.4 g/cm<sup>3</sup> were used for the massive  
482 sulfide lens and underlying crust, respectively, derived from modelling (Evans, 1996) and  
483 sample averages (Ludwig et al., 1998). . As discussed in Graber et al. (2020), a range of densities  
484 have been used to represent the TAG active mound's massive sulfide, from 3.5 g/cm<sup>3</sup> to 3.8  
485 g/cm<sup>3</sup>. Therefore, a reasonable uncertainty on our choice of 3.65 g/cm<sup>3</sup> would be +/- 0.15 g/cm<sup>3</sup>.

486 The 2.4 g/cm<sup>3</sup> density for the background basalt was chosen as it provided the best fit to the data  
487 while performing the Bouguer anomaly regional signal removal. Densities of 2.3 g/cm<sup>3</sup> and 2.5  
488 g/cm<sup>3</sup> provided adequate fits as well, which would result in an effective background uncertainty  
489 of +/- 0.1 g/cm<sup>3</sup>. As the SGI forward solver calculated the gravitational signal of each facet in the  
490 surface model based off the difference in densities across the facet, the uncertainty of the  
491 difference in density between the massive sulfide mound and background basalt will be the sum  
492 of the individual uncertainties, i.e. +/- 0.25 g/cm<sup>3</sup>.

493 Therefore, the eight vertices used to define the massive sulfide layer model resulted in eight  
494 inversion variables. The subsequent SGI took 40 seconds to complete the GA, and 45 minutes to  
495 complete the MCMC sampling.

496 The gravity SGI resulted in a model of the lower surface of the massive sulfide mound,  
497 separating the lens from the altered seafloor crust (Fig. 3d). The volume of rock contained  
498 between the gravity model and the TAG active mound's bathymetric surface then approximates  
499 the volume of massive sulfide contained in the lens. The massive sulfide lens model has an  
500 approximate volume of 594,000 +/- 120,000 m<sup>3</sup>, which would indicate 2.17 +/-0.44 Mt of  
501 material assuming the 3.65 g/cm<sup>3</sup> density used during the modelling, as used in Evans (1996).  
502 Figure 8b shows the SGI results using three density contrasts within the range of +/- 0.25 g/cm<sup>3</sup>  
503 about the chosen 3.65 - 2.4 = 1.25 g/cm<sup>3</sup> contrast. This comparison indicates the uncertainty on  
504 the geometry of the massive sulfide lens resulting from an uncertainty in the chosen density  
505 values.

506

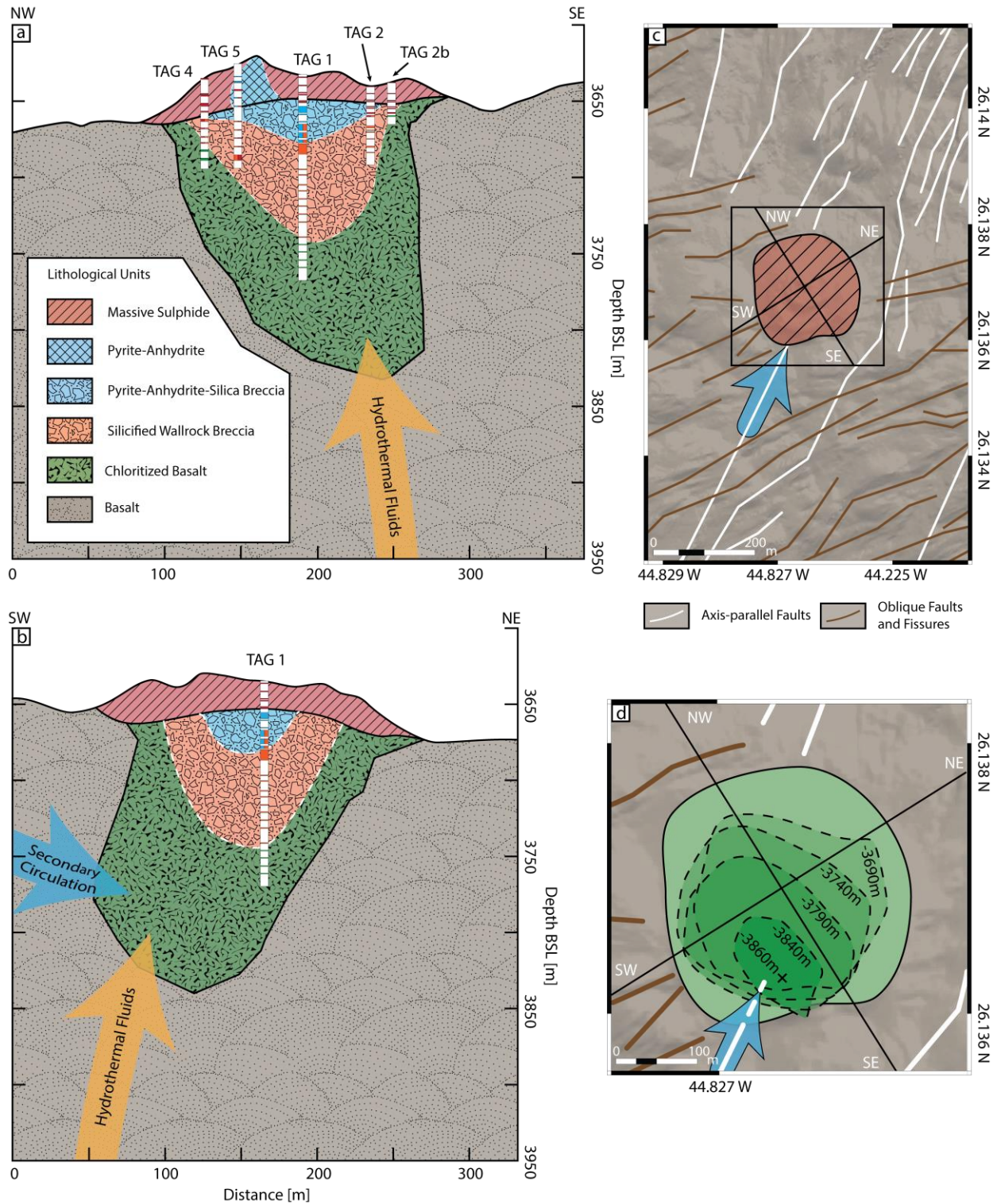
## 507 **5 Discussion**

### 508 **5.1 Updated TAG Geologic Interpretation**

509 The two SGI models produced in this study provide new information on two important aspects of  
510 the TAG active mound: 1) the inversion of the gravity data provides a 3D model for the  
511 thickness of the massive sulfide layer of the deposit; and 2) the inversion of the magnetic data  
512 creates an enclosing surface representing the outer extent of the chlorite-rich hydrothermal  
513 alteration of basalt beneath the deposit. The outer extent of the chloritized basalt will therefore

514 indicate the depth and location of mixing between hydrothermal fluid and seawater at  
515 temperatures greater than 200°C. An updated geologic interpretation, in 3D, was made by  
516 combining the SGI surfaces with inferred interface information from the drillcore (Fig. 9).

517



518

519 **Figure 9.** Two geological cross sections of the TAG active mound derived through gravity and  
 520 magnetic geophysical inverse modelling and drillcore information. The cross-section **a** is  
 521 oriented parallel to the drillholes and **b** orthogonal to them. Dotted white lines indicate

522 surfaces derived from the rock samples retrieved through drilling, and the solid black lines  
523 represent the surfaces created through SGI modelling. In both cross-sections the white space  
524 along the drillholes represents locations with zero recovery. **c** shows a plan view of the deposit  
525 with the interpreted vector for secondary circulation of seawater. **d** a zoomed in plan view of the  
526 deposit showing the isolines of the chloritized basalt surface's depth, with its maximum depth  
527 depicted with an "x".

528

529 Although the ODP Leg 158 drillholes were used to design the initial mode for the SGIs, their  
530 information did not bias results or influence the inversions once they started. The initial models  
531 provided a geometry and topology that should be somewhat close to the actual form of the active  
532 mound's rock units, but once the inversions began the models' vertices moved within their  
533 positional constraints without influence from the initial model. The drillcore information was  
534 used to decide what background magnetic susceptibility to use, as multiple susceptibility values  
535 were used to construct a suite of SGI models but only the 0.08 SI background model was both  
536 statistically appropriate as a background value as well as agreed with the drillcore. There were no  
537 chloritized basalt-basalt intersections in the drillcore to compare the magnetic SGI to, but the  
538 gravity SGI surface correlates closely with the bottom most collected massive sulfide samples  
539 (Fig. 9).

## 540 **5.2 Magnetic SGI Interpretations**

541 The chloritized basalt model, which extends to ~150 m below the seafloor, indicates infiltration  
542 of local seawater (i.e. secondary circulation; Fig. 9) that approaches the base of the mound from  
543 the South-West in line with the axis-parallel faulting passing through the mound (Fig. 1a).  
544 Pontbriand & Sohn (2014) determined a similar geometry for the secondary circulation through  
545 mapping the location of micro seismic events attributed to the precipitation of anhydrite at the  
546 locations of local seawater infiltration near the TAG mound. Their results showed a zone of high  
547 seismic event density to the immediate South-West of the mound, from the near surface to a  
548 depth of 125 m below the seafloor. This suggests that although the rising hydrothermal fluids are  
549 assumed to be approaching from the north-west on the regional scale (normal to the spreading  
550 axis; Szitkar et al., 2015), the locally infiltrating seawater and near surface component of the

551 upflow zone approaches the active mound along axis parallel faulting. The axis parallel faulting  
552 is present at both the North and South of the TAG mound, but the southern faults are heavily  
553 cross-cut by axis-oblique faults and fissures (Fig. 1a).

554 Comparing the geometry of the modelled chloritized basalt unit to ancient VMS systems,  
555 primarily Cyprus-type deposits that have relatively undeformed alteration zones, the chlorite  
556 alteration units can have a range of thicknesses. The thicknesses of the units at the Mathiati  
557 deposit are 10-50 m, and 100-200 m thick at the Skouriotissa deposit (Hannington et al., 1998).  
558 These thicknesses are proportional to the size of the deposits, as a larger ore lens relates to a  
559 larger stockwork system, but they do compare to the 10-75 m thick modelled chloritized basalt  
560 unit for the TAG active mound.

561 Our magnetic modelling assumed that all significant magnetization in the crust around the TAG  
562 active mound was parallel to the Earth's inducing field, although some previous studies have  
563 suggested that remanent magnetization oblique to the Earth's field might be present. Szitkar &  
564 Dymant (2015) found through magnetic forward modelling that the crustal magnetization under  
565 the TAG mound was rotated from the International Geomagnetic Reference Field's (IGRF) 42°  
566 inclination and -15° declination to a 10° inclination and 0° declination. This 53° rotation of the  
567 crust's magnetization about an axis parallel to the Mid-Ocean Ridge axis was inferred to be  
568 caused by the detachment fault tectonics in the region. To consider the presence of remanent  
569 magnetization oblique to the Earth's inducing field vector a TMVI model was created to study  
570 any significant deviations of the model's magnetization vectors (Fig. S3). The results indicated  
571 that the models showed a strong preference to have their magnetization in-line with the IGRF  
572 vector, with small groupings of cells containing oblique magnetizations, with respect to the  
573 IGRF, being associated with overfitting of the data. The effective magnetic susceptibility TMVI  
574 model contains less heterogeneities in the crust surrounding the TAG active mound, as given  
575 more degrees of freedom (i.e. effective magnetic susceptibility, inclination and declination,  
576 versus simply effective magnetic susceptibility as in the scalar magnetic inversion model) the

577 TMVI program used near-surface variations from the IGRF direction to better fit the data rather  
578 than varying purely the effective magnetic susceptibility.

### 579 **5.3 Composition of the active TAG mound from Gravity SGI Modelling**

580 Using the massive sulfide lens gravity SGI model, the volume of rock contained between it and  
581 the overlying bathymetric surface was calculated to be 595,000 m<sup>3</sup> +/- 20%. The derived tonnage  
582 of 2.17 +/-0.44 Mt of rock is in agreement with Graber et al., (2020)'s 2.27 Mt approximation,  
583 which was measured by placing an interpolated surface through the TAG mound to separate the  
584 unit of massive sulfide from the altered crust (Jamieson et al., 2014) and assuming a 3.5 g/cm<sup>3</sup>  
585 density. If 3.65 g/cm<sup>3</sup> was assumed for the density in Graber et al., (2020)'s it would have  
586 resulted in 2.37 Mt, still in agreement with 2.17 +/-0.44 Mt. As seen in Figure 3d, the base of the  
587 massive sulfide lens matches closely with the form of the surrounding bathymetric surface, most  
588 notably observed by the raised region in the center of the mound aligning with the raised pillow  
589 mound terrain noted in Graber et al. (2020). The other study that approximated the massive  
590 sulfide tonnage in the TAG active mound was Hannington et al. (1998), that used a blocky model  
591 of cylindrical units. Their calculated tonnage was 2.7 Mt for the massive sulfide lens, higher than  
592 the value derived from this study's model and that of Graber et al. (2020). This is most likely  
593 caused by the relatively large size of the units in the blocky model adding extra volume as the  
594 five cylinders at the top of the model could not accurately fit the active mound's topography.  
595 Additionally, Hannington et al. (1998) used a 3.8 g/cm<sup>3</sup> density in their calculations; if 3.65  
596 g/cm<sup>3</sup> was used as in this study their tonnage would be 2.6 Mt.

597 In analysis of the geometry of the massive sulfide mound's inversion model, the downward  
598 concavity of the mound's base implies that the replacement alteration of the seafloor below the  
599 mound did not significantly increase its density. The alteration below the mound is composed of  
600 basalt brecciated with veins of silicate, sulfide, and sulfate minerals. The density for these lower  
601 alteration units and the background basalt used in this study was 2.4 +/- 0.1g/cm<sup>3</sup>. Since the  
602 density of the replacement alteration units appears similar to the unaltered basalt, it would imply  
603 that there is not a significant amount of higher density massive sulfide present in that region.  
604 However, this would contradict the samples collected from ODP Leg 158 which recorded  
605 average of 34 % composition of pyrite in the pyrite-anhydrite-silica breccia and the silicified

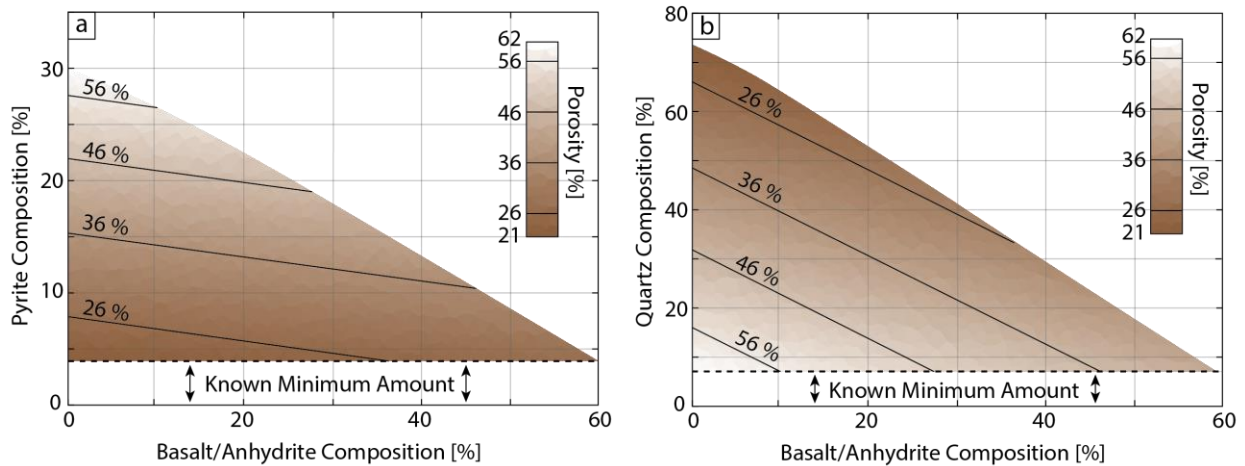
606 wallrock breccia units (Ludwig et al., 1998). A possible explanation for the density of altered  
 607 seafloor is that the drillcore recovery efficiency, which was 12% in Leg 158 (Humphris & Tivey,  
 608 2000), is biased towards intervals that contain abundant higher density sulfide minerals. The  
 609 higher density intervals would not crumble so easily during the drilling and would remain intact  
 610 during retrieval. There might therefore be a lower amount of pyrite present in the seafloor below  
 611 the massive sulfide lens than the Leg 158 drilling suggests. Of the stockwork samples recovered  
 612 during the Leg 158 drilling, their mean percent composition was 34 % sulfide, 4.5 % anhydrite,  
 613 58 % quartz, and 3 % clay (Ludwig et al., 1998). Treating the composition of the recovered  
 614 stockwork core as only representative of 12 % of the stockwork zone, a geologic model of the  
 615 remaining 88 % was constructed to determine its composition. The model is made up of  
 616 percentages of pyrite (5 g/cm<sup>3</sup>; Sharma, 1997), quartz (2.65 g/cm<sup>3</sup>; Sharma, 1997),  
 617 anhydrite/basalt (2.9 g/cm<sup>3</sup>; Sharma, 1997) and pore fluid (0.9 g/cm<sup>3</sup>; Bischoff & Pitzer, 1985),  
 618 while constrained by the modeled bulk density of the stockwork zone (2.4 g/cm<sup>3</sup>) and that the  
 619 percentages of the minerals and porosity sum to 100 %,

$$2.4 \text{ g/cm}^3 = \%_{\text{pyrite}} \cdot (5 \text{ g/cm}^3) + \%_{\text{quartz}} \cdot (2.65 \text{ g/cm}^3) + \%_{\text{basalt}} \cdot (2.9 \text{ g/cm}^3) + \%_{\text{porosity}} \cdot (0.9 \text{ g/cm}^3) \quad 7$$

$$100\% = \%_{\text{pyrite}} + \%_{\text{quartz}} + \%_{\text{basalt}} + \%_{\text{porosity}} \quad 8$$

620 As seen in Fig. 10, the indicated upper bound of pyrite possible in the stockwork zone would be  
 621 30 % (at a porosity of 63 %), with the lower bound being the 4.1 % already observed in the  
 622 drillcore. It is unlikely that the stockwork zone's alteration would greatly increase its porosity,  
 623 with some studies indicating that the alteration instead decreases porosity with the precipitation  
 624 of sulfides, sulfates, and silicates (Wilkins et al., 1991; Zhu et al., 2007). Therefore, the percent  
 625 volume of pyrite in the stockwork zone might be better constrained by considering porosities  
 626 equal to or less than the background basalt's 26 %. This would indicate that at most 7.9 % of the

627 stockwork zone would be composed of pyrite, occurring when there is zero basalt or anhydrite  
 628 remaining and the alteration zone is solely sulfides and silicates.



629

630 **Figure 10.** A geologic model of the percent composition of pyrite, quartz, basalt/anhydrite, and  
 631 pore fluid that makes up the TAG active mound's stockwork zone, derived from Eq. 7 and 8. **a)** a  
 632 plot showing the percent composition of pyrite versus the composition of basalt/anhydrite, with  
 633 each black line representing a constant porosity, at intervals of 10 % from the background value  
 634 of 26 %. **b)** the same style of plot for quartz versus basalt/anhydrite. Viewing **a**, the amount of  
 635 quartz for a given percent amount of pyrite, basalt/anhydrite, and pore fluid can be calculated  
 636 using Eq. 8, with the amount of pyrite being found the same way with **b** and Eq. 8.

637 A limitation of the gravity and magnetic modelling of SMS deposits is the inability of these data  
 638 to resolve the size and geometry of the silicified wallrock stockwork breccia zone below the  
 639 massive sulfide lens. This zone may contain a significant portion of the deposit's precious and  
 640 base metals and determining its volume would be of economic importance. Future work should  
 641 combine the gravity and magnetic modelling with CSEM surveying (e.g. Gehrman et al., 2019;

642 Haroon et al., 2018) and seismic modelling (e.g. Murton et al., 2019) to also resolve the  
643 stockwork zone.

644

## 645 **6 Conclusions**

646 With the use of surface geometry inversion, sparse drilling and minimum-structure inversion  
647 results was further refined to develop a more comprehensive 3D wireframe geologic model of  
648 the TAG active mound. These wireframe models are composed of surfaces representing the  
649 discrete contacts between different rock units, which, in the case of the TAG active mound, was  
650 the interface between the massive sulfide lens and the underlying altered basalt, and the interface  
651 between the chloritized basalt and the unaltered/minimally altered background basalt. Our  
652 gravity inversion model presented a 2.17 +/- 0.44 Mt massive sulfide estimate for anhydrite  
653 contained in the deposit's mound, and the magnetic inversion modelled the maximum depth  
654 where infiltrating seawater mixes with the rising hydrothermal fluids. The model is however  
655 limited in its inability to resolve the geometry of the deposit's silicified wallrock breccia zone,  
656 due to a lack of density or magnetic susceptibility contrast, but through the future integration of  
657 other geophysical surveying methods this could be amended.

## 658 **Acknowledgments**

659 We would like to thank the captain, crew and scientific team from the 2016 R/V Meteor M127  
660 and 1994 R/V Yokosuka MODE'94 cruises for all their work collecting the data modelled in this  
661 study. C.G. are funded through an NSERC Discovery Grant and Memorial University's School  
662 of Graduate Studies Grant. The bathymetric and magnetic data is available from Petersen et al.  
663 (2019) (<https://doi.pangaea.de/10.1594/PANGAEA.899415>) and the gravity data is available  
664 from the Marine Geoscience Data System database (DOI: 10.26022/IEDA/330210). The

665 inversion software used to create the models for this study is property of Memorial University of  
666 Newfoundland and is available upon request from the authors.

667

## 668 **Bibliography**

669 Bischoff, J. L., & Pitzer, K. S. (1985). Phase relations and adiabats in boiling seafloor  
670 geothermal systems. *Earth and Planetary Science Letters*, 75(4), 327–338.

671 [https://doi.org/10.1016/0012-821X\(85\)90177-3](https://doi.org/10.1016/0012-821X(85)90177-3)

672 Bouligand, C., Tivey, M. A., Finn, C. A., Morgan, L. A., Shanks, W. C. P., & Sohn, R. A.  
673 (2020). Geological and Thermal Control of the Hydrothermal System in Northern  
674 Yellowstone Lake: Inferences From High-Resolution Magnetic Surveys. *Journal of*  
675 *Geophysical Research: Solid Earth*, 125(9). <https://doi.org/10.1029/2020JB019743>

676 Caratori Tontini, F., De Ronde, C. E. J., Yoerger, D., Kinsey, J., & Tivey, M. (2012). 3-D  
677 focused inversion of near-seafloor magnetic data with application to the Brothers volcano  
678 hydrothermal system, Southern Pacific Ocean, New Zealand. *Journal of Geophysical*  
679 *Research: Solid Earth*, 117(10), 1–12. <https://doi.org/10.1029/2012JB009349>

680 Constable, S. C., Parker, R. L., & Constable, C. G. (1987). Occam's inversion: A practical  
681 algorithm for generating smooth models from electromagnetic sounding data. *Geophysics*,  
682 52(3), 289–300.

683 Evans, R. L. (1996). A seafloor gravity profile across the TAG hydrothermal mound.  
684 *Geophysical Research Letters*, 23(23), 3447–3450. <https://doi.org/10.1029/96GL00734>

685 Farquharson, C. G., & Lelièvre, P. G. (2017). Modelling and Inversion for Mineral Exploration  
686 Geophysics: A Review of Recent Progress, the Current State-of-the-Art, and Future  
687 Directions. *Proceedings of Exploration 17: Sixth Decennial International Conference on*  
688 *Mineral Exploration*, 17, 51–74. [http://www.dmec.ca/getattachment/7caa09d0-cfd7-4248-](http://www.dmec.ca/getattachment/7caa09d0-cfd7-4248-ab1d-53b67ca65f24/Resources/Exploration-17/Modelling-and-Inversion-for-Mineral-Exploration-Ge.aspx)  
689 [ab1d-53b67ca65f24/Resources/Exploration-17/Modelling-and-Inversion-for-Mineral-](http://www.dmec.ca/getattachment/7caa09d0-cfd7-4248-ab1d-53b67ca65f24/Resources/Exploration-17/Modelling-and-Inversion-for-Mineral-Exploration-Ge.aspx)  
690 [Exploration-Ge.aspx](http://www.dmec.ca/getattachment/7caa09d0-cfd7-4248-ab1d-53b67ca65f24/Resources/Exploration-17/Modelling-and-Inversion-for-Mineral-Exploration-Ge.aspx)

- 691 Galley, A. G., & Koski, R. A. (1999). Setting and characteristics of ophiolite-hosted  
692 volcanogenic massive sulphide deposits. *Reviews in Economic Geology*, 8, 221–246.
- 693 Galley, A., Hannington, M. D., & Jonasson, I. (2007). Volcanogenic massive sulphide deposits.  
694 Mineral deposits of Canada: A synthesis of major deposit-types, district metallogeny, the  
695 evolution of geological provinces, and exploration methods: Geological Association of  
696 Canada. *Mineral Deposits Division, Special Publication.*, 5(6), 141–161.
- 697 Galley, C. G., Jamieson, J. W., Lelièvre, P. G., Farquharson, C. G., & Parianos, J. M. (2020).  
698 Magnetic imaging of seafloor hydrothermal fluid circulation pathways. *Science*  
699 *Advances*, 6(44), 1–11. <https://doi.org/10.1126/sciadv.abc6844>
- 700 Galley, C. G., Lelièvre, P. G., & Farquharson, C. G. (2020). Geophysical inversion for 3D  
701 contact surface geometry. *Geophysics*, 85(6), 1–76. <https://doi.org/10.1190/geo2019-0614.1>
- 702 Gehrman, R. A. S., North, L. J., Graber, S., Sztikar, F., Petersen, S., Minshull, T. A., & Murton,  
703 B. J. (2019). Marine Mineral Exploration With Controlled Source Electromagnetics at the  
704 TAG Hydrothermal Field, 26°N Mid-Atlantic Ridge. *Geophysical Research Letters*, 46(11),  
705 5808–5816. <https://doi.org/10.1029/2019GL082928>
- 706 Graber, S., Petersen, S., Yeo, I., Sztikar, F., Klischies, M., Jamieson, J., Hannington, M.,  
707 Rothenbeck, M., Wenzlaff, E., Augustin, N., & Stobbs, I. (2020). Structural Control,  
708 Evolution, and Accumulation Rates of Massive Sulfides in the TAG Hydrothermal Field.  
709 *Geochemistry, Geophysics, Geosystems*, 21(9). <https://doi.org/10.1029/2020GC009185>
- 710 Grant, H. L. J., Hannington, M. D., Petersen, S., Frische, M., & Fuchs, S. H. (2018). Constraints  
711 on the behavior of trace elements in the actively-forming TAG deposit, Mid-Atlantic Ridge,  
712 based on LA-ICP-MS analyses of pyrite. *Chemical Geology*, 498(July), 45–71.  
713 <https://doi.org/10.1016/j.chemgeo.2018.08.019>
- 714 Hannington, M. D., Galley, A. G., Herzig, P. M., & Petersen, S. (1998). Comparison of the TAG  
715 mound and stockwork complex with Cyprus-type massive sulfide deposits. *Proceedings of*  
716 *the Ocean Drilling Program: Scientific Results*, 158, 389–415.  
717 <https://doi.org/10.2973/odp.proc.sr.158.217.1998>

- 718 Hannington, M., Jamieson, J., Monecke, T., Petersen, S., & Beaulieu, S. (2011). The abundance  
719 of seafloor massive sulfide deposits. *Geology*, *39*(12), 1155–1158.  
720 <https://doi.org/10.1130/G32468.1>
- 721 Haroon, A., Hölz, S., Gehrman, R. A. S., Attias, E., Jegen, M., Minshull, T. A., & Murton, B. J.  
722 (2018). Marine dipole-dipole controlled source electromagnetic and coincident-loop  
723 transient electromagnetic experiments to detect seafloor massive sulphides: Effects of three-  
724 dimensional bathymetry. *Geophysical Journal International*, *215*(3), 2156–2171.  
725 <https://doi.org/10.1093/gji/ggy398>
- 726 Herzig, P. M., & Hannington, M. D. (1995). Polymetallic massive sulfides at the modern  
727 seafloor a review. *Ore Geology Reviews*, *10*(2), 95–115. [https://doi.org/10.1016/0169-](https://doi.org/10.1016/0169-1368(95)00009-7)  
728 [1368\(95\)00009-7](https://doi.org/10.1016/0169-1368(95)00009-7)
- 729 Honsho, C., Ura, T., & Kim, K. (2013). Deep-sea magnetic vector anomalies over the Hakurei  
730 hydrothermal field and the Bayonnaise knoll caldera, Izu-Ogasawara arc, Japan. *Journal of*  
731 *Geophysical Research: Solid Earth*, *118*(10), 5147–5164.  
732 <https://doi.org/10.1002/jgrb.50382>
- 733 Honsho, C., Ura, T., & Tamaki, K. (2012). The inversion of deep-sea magnetic anomalies using  
734 Akaike's Bayesian information criterion. *Journal of Geophysical Research: Solid Earth*,  
735 *117*(1), 1–12. <https://doi.org/10.1029/2011JB008611>
- 736 Humphris, S. E., Alt, J. C., Teagle, D. A. H., & Honnorez, J. J. (1998). Geochemical changes  
737 during hydrothermal alteration of basement in the stockwork beneath the active TAG  
738 hydrothermal mound. *Proceedings of the Ocean Drilling Program: Scientific Results*, *158*,  
739 255–276. <https://doi.org/10.2973/odp.proc.sr.158.220.1998>
- 740 Humphris, S. E., & Tivey, M. K. (2000). A synthesis of geological and geochemical  
741 investigations of the TAG hydrothermal field: Insights into fluid-flow and mixing processes  
742 in a hydrothermal system. *Special Papers-Geological Society of America*, *349*, 213–235.
- 743 Humphris, Susan E., Herzig, P. M., Miller, D. J., Alt, J. C., Becker, K., Brown, D., Brüggmann,  
744 G., Chiba, H., Fouquet, Y., Gemell, J. B., Guerin, G., Hannington, M. D., Holm, N. G.,

- 745 Honnorez, J. J., Iturrino, G. J., Knott, R., Ludwig, R., Nakamura, K., Petersen, S., ... Zhao,  
746 X. (1995). The internal structure of an active sea-floor massive sulphide deposit. *Nature*,  
747 377(6551), 713–716. <https://doi.org/10.1038/377713a0>
- 748 Ishihara, T., Shinohara, M., Fujimoto, H., Kanazawa, T., Araya, A., Yamada, T., Iizasa, K.,  
749 Tsukioka, S., Omika, S., Yoshiume, T., Mochizuki, M., & Uehira, K. (2018). High-  
750 resolution gravity measurement aboard an autonomous underwater vehicle. *Geophysics*,  
751 83(6), G119–G135. <https://doi.org/10.1190/geo2018-0090.1>
- 752 Jamieson, J. W., Clague, D. A., & Hannington, M. D. (2014). Hydrothermal sulfide  
753 accumulation along the Endeavour Segment, Juan de Fuca Ridge. *Earth and Planetary  
754 Science Letters*, 395, 136–148. <https://doi.org/10.1016/j.epsl.2014.03.035>
- 755 Knott, R., Fouquet, Y., Honnorez, J., Petersen, S., & Bohn, M. (1998). Petrology of  
756 hydrothermal mineralization: a vertical section through the TAG mound. *Proceedings of the  
757 Ocean Drilling Program: Scientific Results*, 158, 5–26.  
758 <https://doi.org/10.2973/odp.proc.sr.158.201.1998>
- 759 Kowalczyk, P. (2011). Geophysical exploration for submarine massive sulfide deposits.  
760 *OCEANS'11 - MTS/IEEE Kona, Program Book*.  
761 <https://doi.org/10.23919/oceans.2011.6107069>
- 762 Lelièvre, P. G., Carter-McAuslan, A. E., Dunham, M. W., Jones, D. J., Nalepa, M., Squires, C.  
763 L., Tycholiz, C. J., Vallée, M. A., & Farquharson, C. G. (2018). FacetModeller: Software  
764 for manual creation, manipulation and analysis of 3D surface-based models. *SoftwareX*, 7,  
765 41–46. <https://doi.org/10.1016/j.softx.2018.02.002>
- 766 Lelièvre, P. G., Carter-McAuslan, A., Farquharson, C. G., & Hurich, C. (2012). Unified  
767 geophysical and geological 3D Earth models. *The Leading Edge*, 31(3), 249–368.  
768 <https://doi.org/https://doi.org/10.1190/1.3694900>
- 769 Lelièvre, P. G., & Farquharson, C. G. (2013). Gradient and smoothness regularization operators  
770 for geophysical inversion on unstructured meshes. *Geophysical Journal International*,  
771 195(1), 330–341. <https://doi.org/10.1093/gji/ggt255>

- 772 Lelièvre, P. G., & Oldenburg, D. W. (2009). A 3D total magnetization inversion applicable when  
773 significant, complicated remanence is present. *Geophysics*, *74*(3).  
774 <https://doi.org/10.1190/1.3103249>
- 775 Li, Y., & Oldenburg, D. (2000). Joint inversion of surface and borehole magnetic amplitude data.  
776 *Geophysics*, *65*(2), 540–552. <https://doi.org/10.6038/cjg2018L0618>
- 777 Li, Y., & Oldenburg, D. W. (1998). Separation of regional and residual magnetic field data.  
778 *Geophysics*, *63*(2), 791–794. <https://doi.org/10.1190/1.1887567>
- 779 Ludwig, R. J., Iturrino, G. J., & Rona, P. A. (1998). Seismic velocity-porosity relationship of  
780 sulfide, sulfate, and basalt samples from the TAG hydrothermal mound. *Proceedings of the*  
781 *Ocean Drilling Program: Scientific Results*, *158*, 313–327.  
782 <https://doi.org/10.2973/odp.proc.sr.158.225.1998>
- 783 Murton, B. J., Lehrmann, B., Dutrieux, A. M., Martins, S., de la Iglesia, A. G., Stobbs, I. J.,  
784 Barriga, F. J. A. S., Bialas, J., Dannowski, A., Vardy, M. E., North, L. J., Yeo, I. A. L. M.,  
785 Lusty, P. A. J., & Petersen, S. (2019). Geological fate of seafloor massive sulphides at the  
786 TAG hydrothermal field (Mid-Atlantic Ridge). *Ore Geology Reviews*, *107*(October 2018),  
787 903–925. <https://doi.org/10.1016/j.oregeorev.2019.03.005>
- 788 Okabe, M. (1979). Analytical Expressions for Gravity Anomalies Due To Homogeneous  
789 Polyhedral Bodies and Translations Into Magnetic Anomalies. *Geophysics*, *44*(4), 730–741.  
790 <https://doi.org/10.1190/1.1440973>
- 791 Parker, R. L., & Huestis, S. P. (1974). The inversion of magnetic anomalies in the presence of  
792 topography. *Journal of Geophysical Research*, *79*(11), 1587–1593.  
793 <https://doi.org/10.1029/jb079i011p01587>
- 794 Petersen, S., Herzig, P. M., & Hannington, M. D. (2000). Third dimension of a presently forming  
795 VMS deposit: TAG hydrothermal mound, Mid-Atlantic Ridge, 26°N. *Mineralium Deposita*,  
796 *35*(2–3), 233–259. <https://doi.org/10.1007/s001260050018>
- 797 Petersen, Sven. (2016). *RV METEOR Fahrtbericht / Cruise Report M127 - Extended Version:*  
798 *Metal fluxes and Resource Potential at the Slow-spreading TAG Midocean Ridge Segment*

- 799 (26°N, MAR) – *Blue Mining@Sea*. 32(32), 163.
- 800 Pontbriand, C., & Sohn, R. (2014). Microearthquake evidence for reaction-driven cracking  
801 within the Trans-Atlantic Geotraverse active hydrothermal deposit. *AGU: Journal of*  
802 *Geophysical Research, Solid Earth*, 120, 1195–1209.  
803 <https://doi.org/10.1002/2014JB011376>.Received
- 804 Rona, P. A., Hannington, M. D., Raman, C. V., Thompson, G., Tivey, M. K., Humphris, S. E.,  
805 Lalou, C., & Petersen, S. (1993). Active and relict sea-floor hydrothermal mineralization at  
806 the TAG hydrothermal field, mid-Atlantic ridge. *Economic Geology*, 88(8), 1989–2017.  
807 <https://doi.org/10.2113/gsecongeo.88.8.1989>
- 808 Seyfried, W. E., & Bischoff, J. L. (1981). Experimental seawater-basalt interaction at 300°C, 500  
809 bars, chemical exchange, secondary mineral formation and implications for the transport of  
810 heavy metals. *Geochimica et Cosmochimica Acta*, 45(2), 135–147.  
811 [https://doi.org/10.1016/0016-7037\(81\)90157-5](https://doi.org/10.1016/0016-7037(81)90157-5)
- 812 Sharma, P. V. (1997). *Environmental and engineering geophysics*. Cambridge university press.
- 813 Shewchuk, J. R. (1996). Triangle: Engineering a 2D quality mesh generator and delaunay  
814 triangulator. *Lecture Notes in Computer Science (Including Subseries Lecture Notes in*  
815 *Artificial Intelligence and Lecture Notes in Bioinformatics)*, 1148(February 1970), 203–222.  
816 <https://doi.org/10.1007/bfb0014497>
- 817 Si, H. (2015). TetGen, a delaunay-based quality tetrahedral mesh generator. *ACM Transactions*  
818 *on Mathematical Software*, 41(2). <https://doi.org/10.1145/2629697>
- 819 Smith, S. E., & Humphris, S. E. (1998). Geochemistry of basaltic rocks from the TAG  
820 hydrothermal mound (26°08'N), Mid-Atlantic Ridge. *Proceedings of the Ocean Drilling*  
821 *Program: Scientific Results*, 158, 213–229.  
822 <https://doi.org/10.2973/odp.proc.sr.158.218.1998>
- 823 Szitkar, F., & Dymant, J. (2015). Near-seafloor magnetics reveal tectonic rotation and deep  
824 structure at the TAG (Trans-Atlantic Geotraverse) hydrothermal site (Mid-Atlantic Ridge,  
825 26°N). *Geology*, 43(1), 87–90. <https://doi.org/10.1130/G36086.1>

- 826 Szitkar, F., Dyment, J., Choi, Y., & Fouquet, Y. (2014). What causes low magnetization at  
827 basalt-hosted hydrothermal sites? Insights from inactive site Krasnov (MAR 16°38'N).  
828 *Geochemistry, Geophysics, Geosystems*, *15*(4), 1441–1451.  
829 <https://doi.org/10.1002/2014GC005284>
- 830 Szitkar, F., Petersen, S., Tontini, F. C., & Cocchi, L. (2015). High-resolution magnetics reveal  
831 the deep structure of a volcanic-arc-related basalt-hosted hydrothermal site (Palinuro,  
832 Tyrrhenian Sea). *Geochemistry Geophysics Geosystems*, *16*(1), 267–300.  
833 <https://doi.org/10.1002/2014GC005684>.Key
- 834 Tivey, M. A., Rona, P. A., & Schouten, H. (1993). Reduced crustal magnetization beneath the  
835 active sulfide mound, TAG hydrothermal field, Mid-Atlantic Ridge at 26°N. *Earth and*  
836 *Planetary Science Letters*, *115*(1–4), 101–115. [https://doi.org/10.1016/0012-](https://doi.org/10.1016/0012-821X(93)90216-V)  
837 [821X\(93\)90216-V](https://doi.org/10.1016/0012-821X(93)90216-V)
- 838 Tivey, M. A., Schouten, H., & Kleinrock, M. C. (2003). A near-bottom magnetic survey of the  
839 Mid-Atlantic Ridge axis at 26°N: Implications for the tectonic evolution of the TAG  
840 segment. *Journal of Geophysical Research: Solid Earth*, *108*(B5), 1–13.  
841 <https://doi.org/10.1029/2002jb001967>
- 842 Wang, S., Chang, L., Wu, T., & Tao, C. (2020). Progressive Dissolution of Titanomagnetite in  
843 High-Temperature Hydrothermal Vents Dramatically Reduces Magnetization of Basaltic  
844 Ocean Crust. *Geophysical Research Letters*, *47*(8), 1–11.  
845 <https://doi.org/10.1029/2020GL087578>
- 846 Wilkens, R. H., Fryer, G. J., & Karsten, J. (1991). Evolution of porosity and seismic structure of  
847 upper oceanic crust: importance of aspect ratios. *Journal of Geophysical Research*,  
848 *96*(B11). <https://doi.org/10.1029/91jb01454>
- 849 You, C. F., & Bickle, M. J. (1998). Evolution of an active sea-floor massive sulphide deposit.  
850 *Nature*, *394*(6694), 668–671. <https://doi.org/10.1038/29279>
- 851 Zhao, X., Housen, B., Solheid, P., & Xu, W. (1998). Magnetic Properties of Leg 158 cores: the  
852 origin of remanence and its relation to alteration and mineralization of the active TAG

853 mound. *Proceedings of the Ocean Drilling Program, Scientific Results*, 158, 337–351.

854 Zhu, W., Tivey, M. K., Gittings, H., & Craddock, P. R. (2007). Permeability-porosity  
855 relationships in seafloor vent deposits: Dependence on pore evolution processes. *Journal of*  
856 *Geophysical Research: Solid Earth*, 112(5), 1–15. <https://doi.org/10.1029/2006JB004716>

857

858